Heat transfer enhancement via Görtler flow with spatial numerical simulation

Vinicius Malatesta

Centro Tecnológico de Joinville,
Universidade Federal de Santa Catarina, Joinville, Brazil, and

Josuel Kruppa Rogenski and Leandro Franco de Souza

Departamento de Matemática Aplicada e Estatística,
Universidade de São Paulo, São Carlos, Brazil

Abstract

Purpose – The centrifugal instability mechanism of boundary layers over concave surfaces is responsible for the development of quasi-periodic, counter-rotating vortices aligned in a streamwise direction known as Görtler vortices. By distorting the boundary layer structure in both the spanwise and the wall-normal directions, Görtler vortices may modify heat transfer rates. The purpose of this study is to conduct spatial numerical simulation experiments based on a vorticity–velocity formulation of the incompressible Navier–Stokes system of equations to quantify the role of the transition in the heat transfer process.

Design/methodology/approach – Experiments are conducted using an in-house, parallel, message-passing code. Compact finite difference approximations and a spectral method are used to approximate spatial derivatives. A fourth-order Runge–Kutta method is adopted for time integration. The Poisson equation is solved using a geometric multigrid method.

Findings – Results show that the numerical method can capture the physics of transitional flows over concave geometries. They also show that the heat transfer rates in the late stages of the transition may be greater than those for either laminar or turbulent ones.

Originality/value – The numerical method can be considered as a robust alternative to investigate heat transfer properties in transitional boundary layer flows over concave surfaces.

Keywords Heat transfer enhancement, Incompressible flow, Spectral method,
Compact finite difference approximations, Görtler vortices, Spatial numerical simulation

Paper type Research paper

1. Introduction

The practical interest in intensifying surface heat transfer rates with the least penalty follows the need of reducing energy consumption via more efficient systems (Liu, 2008). The design of such efficient systems demands comprehension of the problem under consideration. Specifically, in thermal boundary layer flows, great advances have been achieved in both theoretical (Saffmann, 1995) and experimental (Fiebig, 1996) fields. Fiebig (1996) analyzed the influence of the generation and development of streamwise vortices on heat transfer rates. It can be observed that vortex generators of the winglet type cause a great loss to the system because, although it can double the rate of heat transfer, it almost quadruples the drag. The author supported that the longitudinal vortices are more effective than the transverse ones for heat transfer enhancement. He also underlined that transverse

vortices may lead the flow to turbulence at lower Reynolds numbers than the longitudinal ones.

The geometry of the wall may also modify the transition process. Imbalances between the centrifugal force and the pressure gradient in the wall-normal direction can anticipate turbulence (Saric, 1994). In boundary layer flows, this centrifugal instability is commonly referred to as the Görtler instability. This instability is important from a practical point of view, as the Görtler vortices may be observed in flows over turbine blades and combustion chambers (Biegger and Weigand, 2015). Görtler vortices are responsible for generating strong distortions in the velocity profiles (Liu and Lee, 1995). As the vortices are counter-rotating, two regions arise between them: the upwash and the downwash regions. The downwash region is responsible for compressing the boundary layer toward to the wall and, as a consequence, for increasing the heat transfer rates. The upwash region does the opposite.

The cross-sectional heat advection distribution obtained with Görtler flow is different from the one obtained with a laminar boundary layer on a flat surface. To explicit these differences, experimental studies were conducted, and they showed that the heat transfer enhancement in Görtler flows can be higher than that observed in turbulent flows (Peerhossaini, 1987). Momayez and Peershossaini (2004) and Momayez et al. (2004) conducted experiments to understand the effects of Görtler vortices and their transition to turbulence on heat transfer from the wall to the boundary layer.

Tandiano et al. (2009) studied the development of wall shear layer stress in a concave surface boundary layer flow in the presence of Görtler vortices. They analyzed the flow by hot-wire measurements, and vertical perturbation wires were adopted to introduce perturbations in a selected wavelength. The authors concluded that the spanwise-averaged wall shear stress coefficient *Cf*, which initially follows the Blasius curve, increases well above the local turbulent boundary layer value further downstream because of the nonlinear effects of Görtler instability and secondary instabilities.

Liu (2008) conducted studies to explain theoretically the rate of heat transfer in a boundary layer flow over a slightly concave surface. His conclusion reaffirms that one may greatly enhance the heat transfer, although paying the price of almost one to one in drag.

Görtler was the first to discuss the evolution of the streamwise vortices. Görtler assumed the problem was locally parallel and applied a normal-mode analysis to discuss how instabilities may occur if a dimensionless parameter (later named as the Görtler number) exceeds a critical value.

In general, numerical studies regarding the evolution of the Görtler vortices rely on normal modes or marching procedures. Historically, different neutral curves were obtained through the local/nonlocal assumption. Remarkable discussions regarding this topic are provided by Floryan and Saric (1982), Hall (1982) and Floryan (1991). A comprehensive discussion about the Görtler instability is provided by Saric (1994).

A parabolized formulation was adopted by Liu and Lee (1995) to numerically study the influence on the Prandtl number in the heat transfer rates of boundary layer flows over a concave wall. They studied flows with three different Prandtl numbers ($Pr = 0.72$, 1.00 and 7.07). The spanwise wavenumber was the same, obtained experimentally by Swearingen and Blackwelder (1987). Their results showed that one could achieve high gains in heat transfer rates in the presence of Görtler vortices. Momayez et al. (2009) support this conclusion and also show that the intensification of heat transfer is related to the growth of Görtler vortices under the effect of centrifugal instability and, secondary instabilities.

Schrader et al. (2011) identify a lack in spatial direct numerical simulation studies of Görtler flow. The authors provided a detailed investigation of the receptivity of the Görtler

boundary layer because of both free-stream turbulence and localized wall roughness. Results provided by them support that receptivity is linear for most of the tested cases and free-stream turbulence is more effective in exciting the vortices than the localized wall roughness. However, heat transfer analysis was not discussed in their paper.

In the present paper, the influence of the centrifugal instability in heat transfer enhancement is investigated using a spatial numerical simulation code. The same physical parameters provided by Mitsudharmadi *et al.* (2004, 2005, 2006) have been adopted. We explicit benefits of the use of high-order finite difference schemes combined to a wall-normal stretching technique to effectively capture the physics of the heat transfer phenomenon in Görtler flows.

2. Formulation
The incompressible, unsteady system of equations with constant density and constant viscosity is chosen to represent the flow of a Newtonian fluid over a concave surface. Defining vorticity as the negative curl of the velocity vector, and using the fact that both the velocity and the vorticity fields are solenoidal, one can obtain the following vorticity transport equations:

$$\frac{\partial \widetilde{\omega}_x}{\partial t} + \frac{\partial \tilde{a}}{\partial y} - \frac{\partial \tilde{b}}{\partial z} + \frac{Go^2}{\sqrt{Re}}\frac{\partial \tilde{d}}{\partial z} = \frac{1}{Re}\nabla^2\widetilde{\omega}_x, \tag{1}$$

$$\frac{\partial \widetilde{\omega}_y}{\partial t} + \frac{\partial \tilde{c}}{\partial z} - \frac{\partial \tilde{a}}{\partial x} = \frac{1}{Re}\nabla^2\widetilde{\omega}_y, \tag{2}$$

$$\frac{\partial \widetilde{\omega}_z}{\partial t} + \frac{\partial \tilde{b}}{\partial x} - \frac{\partial \tilde{c}}{\partial y} - \frac{Go^2}{\sqrt{Re}}\frac{\partial \tilde{d}}{\partial x} = \frac{1}{Re}\nabla^2\widetilde{\omega}_z, \tag{3}$$

where:

$$\tilde{a} = \widetilde{\omega}_x\tilde{v} - \widetilde{\omega}_y\tilde{u}, \tag{4}$$

$$\tilde{b} = \widetilde{\omega}_z\tilde{u} - \widetilde{\omega}_x\tilde{w}, \tag{5}$$

$$\tilde{c} = \widetilde{\omega}_y\tilde{w} - \widetilde{\omega}_z\tilde{v}, \tag{6}$$

$$\tilde{d} = \tilde{u}^2, \tag{7}$$

are the nonlinear terms resulting from convection, vortex stretching, vortex bedding and the curvature influence, respectively. The variables ($\tilde{u}$, $\tilde{v}$, $\tilde{w}$, $\widetilde{\omega}_x$, $\widetilde{\omega}_y$, $\widetilde{\omega}_z$) are the dimensionless velocity and vorticity components in the streamwise (x), wall normal (y) and spanwise (z) directions; t is the time. The ∇^2 operator is as follows:

$$\nabla^2 = \left(\frac{\partial^2}{\partial x^2} + \frac{\partial^2}{\partial y^2} + \frac{\partial^2}{\partial z^2}\right). \tag{8}$$

The continuity equation is given as follows:

$$\frac{\partial \tilde{u}}{\partial x} + \frac{\partial \tilde{v}}{\partial y} + \frac{\partial \tilde{w}}{\partial w} = 0. \tag{9}$$

The adopted heat transfer transport equation is given as follows:

$$\frac{\partial \widetilde{\theta}}{\partial t} + \frac{\partial \widetilde{u}\widetilde{\theta}}{\partial x} + \frac{\partial \widetilde{v}\widetilde{\theta}}{\partial y} + \frac{\partial \widetilde{w}\widetilde{\theta}}{\partial z} = \frac{1}{Re\,Pr}\nabla^2\theta \tag{10}$$

where $\widetilde{\theta}$ is the nondimensional temperature given by $\widetilde{\theta} = (T - T_0)/(T_\infty - T_0)$, where T is the dimensional temperature, and T_∞ and T_0 are the dimensional temperature values that are at a considerable distance from the thermal boundary layer and at the wall, respectively. The reference length is a plate characteristic length L and the reference velocity is the freestream velocity U_∞. The Reynolds number is given by $Re = U_\infty L/\nu$, where ν is the kinematic viscosity. The Görtler number is given by $Go = (K_c\sqrt{Re})^{1/2}$. The terms $Go^2 \partial\widetilde{d}\big/\partial x/\sqrt{Re}$ and $Go^2 \partial\widetilde{d}\big/\partial z/\sqrt{Re}$ are the leading order curvature terms, where $K_c = L/R$ is the wall curvature and R is the curvature radius (Floryan and Saric, 1982). The Prandtl number is given by $Pr = \nu/\alpha$, where α is the thermal diffusivity of the fluid.

Taking the definition of the vorticity and equation (9), one can obtain Poisson-type equations for each velocity component as follows:

$$\frac{\partial^2\widetilde{u}}{\partial x^2} + \frac{\partial^2\widetilde{u}}{\partial z^2} = -\frac{\partial\widetilde{\omega}_y}{\partial z} - \frac{\partial^2\widetilde{v}}{\partial x\partial y}, \tag{11}$$

$$\frac{\partial^2\widetilde{v}}{\partial x^2} + \frac{\partial^2\widetilde{v}}{\partial y^2} + \frac{\partial^2\widetilde{v}}{\partial z^2} = -\frac{\partial\widetilde{\omega}_z}{\partial x} + \frac{\partial\widetilde{\omega}_x}{\partial z}, \tag{12}$$

$$\frac{\partial^2\widetilde{w}}{\partial x^2} + \frac{\partial^2\widetilde{w}}{\partial z^2} = \frac{\partial\widetilde{\omega}_y}{\partial x} - \frac{\partial^2\widetilde{v}}{\partial y\partial z}. \tag{13}$$

2.1 Disturbance formulation
Flow variables $\widetilde{\tau} = \{\widetilde{u}, \widetilde{v}, \widetilde{w}, \widetilde{\omega}_x, \widetilde{\omega}_y, \widetilde{\omega}_z\}$ are decomposed in baseflow and perturbation parts as follows:

$$\widetilde{\tau} = \tau_b + \tau, \tag{14}$$

where subscript b indicates a baseflow quantity. The baseflow is assumed to be two-dimensional, i.e. only u_b, v_b, ω_{zb} and θ_b should be considered. Both baseflow and perturbation quantities are assumed to satisfy the system of equations.

By introducing equation (14) in the equations (1)-(3) and (10)-(13) and by subtracting baseflow quantities, the evolution of disturbances can be represented as follows:

$$\frac{\partial\omega_x}{\partial t} + \frac{\partial a}{\partial y} - \frac{\partial b}{\partial z} + \frac{Go^2}{\sqrt{Re}}\frac{\partial d}{\partial z} = \frac{1}{Re}\nabla^2\omega_x, \tag{15}$$

$$\frac{\partial\omega_y}{\partial t} + \frac{\partial c}{\partial z} - \frac{\partial a}{\partial x} = \frac{1}{Re}\nabla^2\omega_y, \tag{16}$$

$$\frac{\partial\omega_z}{\partial t} + \frac{\partial b}{\partial x} - \frac{\partial c}{\partial y} - \frac{Go^2}{\sqrt{Re}}\frac{\partial d}{\partial x} = \frac{1}{Re}\nabla^2\omega_z, \tag{17}$$

$$\frac{\partial^2 u}{\partial x^2} + \frac{\partial^2 u}{\partial z^2} = -\frac{\partial\omega_y}{\partial z} - \frac{\partial^2 v}{\partial x\partial y}, \tag{18}$$

$$\frac{\partial^2 v}{\partial x^2} + \frac{\partial^2 v}{\partial y^2} + \frac{\partial^2 v}{\partial z^2} = -\frac{\partial \omega_z}{\partial x} + \frac{\partial \omega_x}{\partial z}, \tag{19}$$

$$\frac{\partial^2 w}{\partial x^2} + \frac{\partial^2 w}{\partial z^2} = \frac{\partial \omega_y}{\partial z} - \frac{\partial^2 v}{\partial y \partial z}, \tag{20}$$

$$\frac{\partial \theta}{\partial t} + \frac{\partial e}{\partial x} + \frac{\partial f}{\partial y} + \frac{\partial g}{\partial z} = \frac{1}{Re\,Pr}\nabla^2\theta, \tag{21}$$

$$\frac{\partial u}{\partial x} + \frac{\partial v}{\partial y} + \frac{\partial w}{\partial w} = 0, \tag{22}$$

where the nonlinear terms a, b, c, d, e, f and g are calculated as follows:

$$a = \omega_x(v_b + v) - \omega_y(u_b + u), \tag{23}$$

$$b = (\omega_{zb} + \omega_z)(u_b + u) - \omega_x\,\omega, \tag{24}$$

$$c = \omega_y\omega - (\omega_{xb} + \omega_z)(v_b + v), \tag{25}$$

$$d = 2u_bu + u^2, \tag{26}$$

$$e = u_b\theta + u\theta_b + u\theta, \tag{27}$$

$$f = v_b\theta + v\theta_b + v\theta, \tag{28}$$

$$g = \omega(\theta_b + \theta). \tag{29}$$

The necessary boundary conditions to close the system of equations are discussed in the next section.

3. Numerical method
The system of equations (15)-(22) is solved in a computational domain illustrated in Figure 1. The numerical solution of the Görtler problem follows the procedure described by Kloker *et al.* (1993), Souza *et al.* (2004) and Malatesta *et al.* (2013).

3.1 Spectral approximation
The flow is assumed to be periodic in the spanwise direction. Therefore, flow variables can be represented by the use of $K + 1$ spanwise Fourier modes as follows:

$$\psi(x, y, z, t) = \sum_{k=0}^{K} \Psi_k(x, y, t)e^{i\beta_k z}. \tag{30}$$

where:

$$\psi = \{u,\ v,\ w,\ \omega_x, \omega_y,\ \omega_z,\ \theta,\ a,\ b,\ c,\ d,\ e,\ f, g\},$$

$$\Psi_k = \{U_k,\ V_k,\ W_k,\ \Omega_{xk},\ \Omega_{yk},\ \Omega_{zk},\ \Theta_{zk},\ A_k,\ B_k,\ C_k,\ D_k,\ E_k,\ F_k,\ G_k\},$$

β_k is the spanwise wavenumber given by $\beta_k = 2\pi k/\lambda_z$, λ_z is the spanwise wavelength of the fundamental spanwise Fourier mode and $i = \sqrt{-1}$.
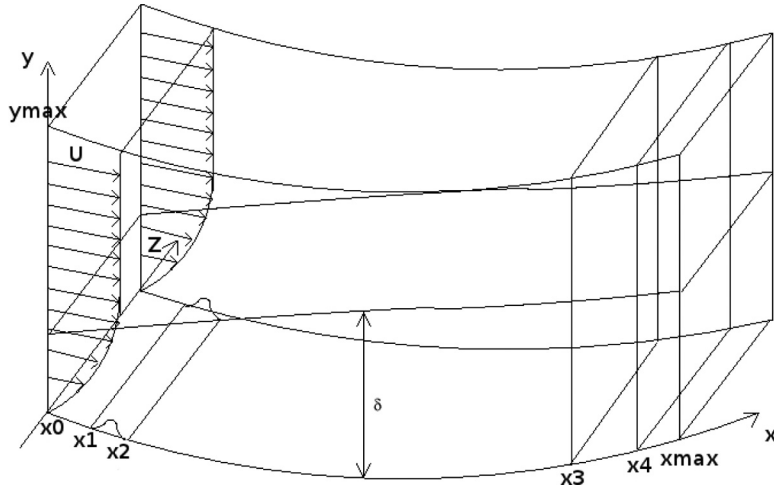
Figure 1.
Computational domain

In this sense, the vorticity transport equations (15)-(17), the velocity Poisson equations (18)-(20) and the heat transfer transport equation (21) can be expressed in the Fourier space (for any k Fourier mode) as follows:

$$\frac{\partial \Omega_{xk}}{\partial t} + \frac{\partial A_k}{\partial y} - \beta_k B_k - \frac{Go^2}{\sqrt{Re}}\beta_k D_k^2 = \frac{1}{Re}\nabla_k^2\Omega_{xk}, \tag{31}$$

$$\frac{\partial \Omega_{yk}}{\partial t} + \beta_k C_k - \frac{\partial A_k}{\partial x} = \frac{1}{Re}\nabla_k^2\Omega_{yk}, \tag{32}$$

$$\frac{\partial \Omega_{zk}}{\partial t} + \frac{\partial B_k}{\partial x} + \frac{\partial C_k}{\partial y} - \frac{Go^2}{\sqrt{Re}}\frac{\partial D_k^2}{\partial x} = \frac{1}{Re}\nabla_k^2\Omega_{zk}, \tag{33}$$

$$\frac{\partial^2 U_k}{\partial x^2} - \beta_k^2 U_k = -\beta_k\Omega_{yk} - \frac{\partial^2 V_k}{\partial x\partial y}, \tag{34}$$

$$\frac{\partial^2 V_k}{\partial x^2} + \frac{\partial^2 V_k}{\partial y^2} - \beta_k^2 V_k = -\frac{\partial \Omega_{zk}}{\partial x} + \beta_k\Omega_{xk}, \tag{35}$$

$$\frac{\partial^2 W_k}{\partial x^2} - \beta_k^2 W_k = \frac{\partial \Omega_{yk}}{\partial x} + \beta_k\frac{\partial V_k}{\partial y}, \tag{36}$$

$$\frac{\partial \Theta_k}{\partial t} + \frac{\partial E_k}{\partial x} + \frac{\partial F_k}{\partial y} - i\beta_k G = \frac{1}{Re\,Pr}\nabla_k^2\Theta_k, \tag{37}$$

where

$$\nabla_k^2 = \left(\frac{\partial^2}{\partial x^2} + \frac{\partial^2}{\partial y^2} - \beta_k^2\right).$$

Equations (31)-(37) are solved numerically in the domain that is shown schematically in Figure 1. The calculations are performed considering an orthogonal and y-stretched grid parallel to the wall. The fluid enters in the computational domain at $x = x_0$ and exits at $x = x_{max}$. Disturbances are introduced into the flow field using spanwise suction and blowing in a strip at the wall. This strip is located between x_1 and x_2. In the region located between x_3 and x_4, a buffer domain technique (Kloker *et al.*, 1993) was implemented to avoid wave reflections at the outflow boundary.

The time derivative in the vorticity transport equations is discretized with a classical fourth-order Runge–Kutta integration scheme. The spatial derivatives are calculated using a high-order compact finite difference scheme shown by Souza *et al.* (2005). The V-Poisson equation – equation (35) – is solved using a multigrid Full Approximation Scheme (Stüben and Trottenberg, 1981). A V-cycle with four levels is implemented (Rogenski *et al.*, 2014).

In these simulations, a two-dimensional Navier–Stokes solution based on the Blasius similar solution is used as the baseflow. The solution is obtained by assuming that the flow quantities are constant in the spanwise direction, i.e. only mode $k = 0$ is taken into account. The simulation is performed until the maximum difference between the spanwise vorticity component at two consecutive time steps is smaller than 10^{-8}.

The code is parallelized through a domain decomposition technique in the streamwise direction. Communications between subdomains are provided by the use of the Message Passing Interface (MPI) library.

3.2 Boundary conditions
The system of governing equations is closed by the specification of boundary conditions. At the wall ($y = 0$), the no-slip condition is imposed for the streamwise (U_k) and the spanwise (W_k) velocity components. The wall-normal velocity component (V_k) is specified at a suction and blowing strip region located between x_1 and x_2, where the disturbances are introduced. Away from the disturbance generator, this velocity component is set to zero. The function used for the wall-normal velocity $V_{k=1}$ is calculated as follows:

$$V_{k=1}(i, 0, t) = A \, sin^3(\varepsilon) \text{ for } x_1 \leq x \leq x_2 \tag{38}$$

where $\epsilon = (x - x_1)/(x_2 - x_1)$ and A is a real constant chosen to adjust the amplitude of the disturbance. The adopted function assures that the wall-normal velocity component and its first and second derivatives are continuous along the wall. For all modes but $k = 1$, $V_k(x, 0, t) = 0$.

At the inflow boundary ($x = x_0$), the velocity, the vorticity components and the temperature are specified based on the similarity solutions. At the outflow boundary ($x = x_{max}$), the second derivatives with respect to the streamwise direction of the velocity and vorticity components are set to zero. At the upper boundary ($y = y_{max}$), the flow is considered nonrotational. The y_{max} position is prescribed by adopting at least three times the boundary layer thickness at the outflow boundary. Setting all vorticity components to zero satisfies the nonrotational condition. The wall-normal velocity component at the upper boundary is settled according to the following condition:

$$\left. \frac{\partial V_k}{\partial y} \right|_{x, y_{max}, t} = 0. \tag{39}$$

This condition is imposed in the solution of the V_k velocity in the Poisson equation (35). The equations used for evaluating the vorticity components at the wall are as follows:

$$\frac{\partial^2\Omega_{xk}}{\partial x^2} - \beta_k^2\Omega_{xk} = -\frac{\partial^2\Omega_{yk}}{\partial x\partial y} - \beta_k\nabla_k^2 V_k, \tag{40}$$

$$\frac{\partial\Omega_{zk}}{\partial x} = \beta_k\Omega_{xk} - \nabla_k^2 V_k. \tag{41}$$

A damping zone near the outflow boundary is defined in which all the disturbances were gradually damped down to zero (Kloker *et al.*, 1993). This technique is used to avoid reflections in the outflow boundary. Meitz and Fasel (2000) adopted a fifth-order polynomial, and the same function is used in the present code. The basic idea is to multiply the vorticity components by a ramp function $f_1(x)$ after each sub-step of the integration method. Using this technique, the disturbance vorticity components are taken as follows:

$$\Omega_k(x, y, t) = f_1(x)\Omega_k^*(x, y, t), \tag{42}$$

where $\Omega_k^*(x,y,t)$ is the disturbance vorticity component that results from the Runge–Kutta integration, and $f_1(x)$ is a ramp function that goes smoothly from 1 to 0. The implemented function is as follows:

$$f_1(x) = f(\epsilon) = 1 - 6\epsilon^5 + 15\epsilon^4 - 10\epsilon^3, \tag{43}$$

where $\epsilon = (x - x_3)/(x_4 - x_3)$ for $x_3 \leq x \leq x_4$. To ensure good numerical results, a minimum distance between x_3 and x_4 and between x_4 and x_{max} has to be adopted (Kloker *et al.*, 1993). In the present simulations, 30 grid points are adopted in each region.

Another buffer domain, located near the inflow boundary, is also implemented in the code. As pointed out by Meitz (1996), in simulations involving streamwise vortices, reflections due to the vortices at the inflow can contaminate the numerical solution. The damping function is similar to the one used for the outflow boundary:

$$f_2(x) = f(\epsilon) = 6\epsilon^5 - 15\epsilon^4 + 10\epsilon^3, \tag{44}$$

where $\epsilon = (x - 1)/(x_1 - 1)$ for $1 \leq x \leq x_1$. All the disturbance vorticity components are multiplied by this function in this region.

The boundary conditions for the disturbance temperature are as follows:

- at the inflow boundary, we impose $\theta_k = 0$;
- at the outflow boundary, we also impose $\theta_k = 0$, as the same buffer domain for vorticity was also applied for the temperature; and
- at the wall, $\theta_k = 0$.

The method and code adopted in the present paper have been validated and verified for the hydrodynamic boundary layer by Malatesta *et al.* (2013).

3.3 Wavenumber analyses of compact finite difference schemes in non-uniform meshes
Following studies of Lele (1992) and Gamet *et al.* (1999), wavenumber Fourier analyses of the spatial finite difference schemes are conducted by considering a single Fourier mode $f(x) = e^{i\tau s}$, where τ is the scaled wavenumber. Analytical first and second derivatives of that mode with respect to x are given by $f' = i\tau f$ and $f'' = -\tau^2 f$.

The use of finite difference schemes to approximate the first derivative of a Fourier mode can be expressed by $f_d' = i\tau'(\tau)f$. In this expression, the function τ' is well known as the

modified wave number. The relation $\tau'(\tau) = \tau$ represents exact differentiation. In the same way, considering that $f_d'' = -\tau''(\tau)f$, numerical second derivatives' errors can be estimated by a distance between τ^2 and τ''.

3.3.1 Resolution of spatial numerical schemes. The high-order compact finite difference approximations are used to calculate spatial-derivative quantities. The first-derivative relation for centered (c) schemes has the following form:

$$\alpha_{k-1}^{(c)}f_{k-1}' + \alpha_k^{(c)}f_k' + \alpha_{k+1}^{(c)}f_{k+1}' + a_{k-2}^{(c)}f_{k-2} + a_{k-1}^{(c)}f_{k-1} + a_k^{(c)}f_k$$
$$+ a_{k+1}^{(c)}f_{k+1} + a_{k+2}^{(c)}f_{k+2} = 0, \tag{45}$$

where $\alpha_k^{(c)}$ and $a_k^{(c)}$ are the finite difference coefficients associated with the stencil position k. The constants for a uniform grid can be found in the study by Lele (1992). Stretching factors of 2 and 5 per cent are also considered for comparison. Compact finite difference coefficients for the centered first-derivative stencil provided by equation (45) with the previous stretching factors are presented in Table I.

Figures 2(a) and (b) show the comparison of the real and imaginary parts of modified wavenumber versus wavenumber for the present approximation. It is worth noting that the real part of the wavenumber is associated with dispersive errors, while the imaginary part is connected with dissipative ones (Lele, 1992).

As can be seen in Figure 2(a), small variations in the stretching factor do not lead to drastic shape variations in the real part of the modified wavenumber. However higher the stretching factors, lesser the set of well-resolved waves. Figure 2b shows that in the uniform mesh case, the modified wavenumber is real-valued, as expected. Inevitably, the loss of symmetry due to the stretch introduces dissipative errors for high wavenumbers.

The second-derivative analysis follows the same form of the previous derivative case. The same comparison taking into account stretching factors of 2 and 5 per cent is considered. Real and imaginary parts of the function τ'' are represented by Figure 3(a) and (b). Table I also presents the compact finite coefficients for the second-derivative approximation.

Coefficients	$sf = 1.00$	1.02	1.05
$\alpha_{k-1}^{(c)}$	0.333333	0.346755	0.367209
$\alpha_k^{(c)}$	1	1	1
$\alpha_{k+1}^{(c)}$	0.333333	0.320348	0.302103
$a_{k-2}^{(c)}$	0.0277778	0.0303514	0.0344917
$a_{k-1}^{(c)}$	0.777778	0.780828	0.784364
$a_k^{(c)}$	0	-0.0576701	-0.136054
$a_{k+1}^{(c)}$	0.777778	-0.729578	-0.663595
$a_{k+2}^{(c)}$	-0.0277778	-0.0239318	-0.0192063
$\beta_{k-1}^{(c)}$	0.181818	0.175976	0.165648
$\beta_k^{(c)}$	1	1	1
$\beta_{k+1}^{(c)}$	0.181818	0.186814	0.192812
$b_{k-2}^{(c)}$	-0.0681818	-0.0651007	-0.0590515
$b_{k-1}^{(c)}$	-1.09091	-1.03894	-0.970319
$b_k^{(c)}$	2.31818	2.18512	2.0062
$b_{k+1}^{(c)}$	-1.09091	-1.01844	-0.922459
$b_{k+2}^{(c)}$	-0.0681818	-0.0626328	-0.0543688

Table I.
Compact finite difference coefficients for a stencil provided by equation (45) with $sf = 1.00$, 1.02 and 1.05

(a)   (b)

(a)   (b)
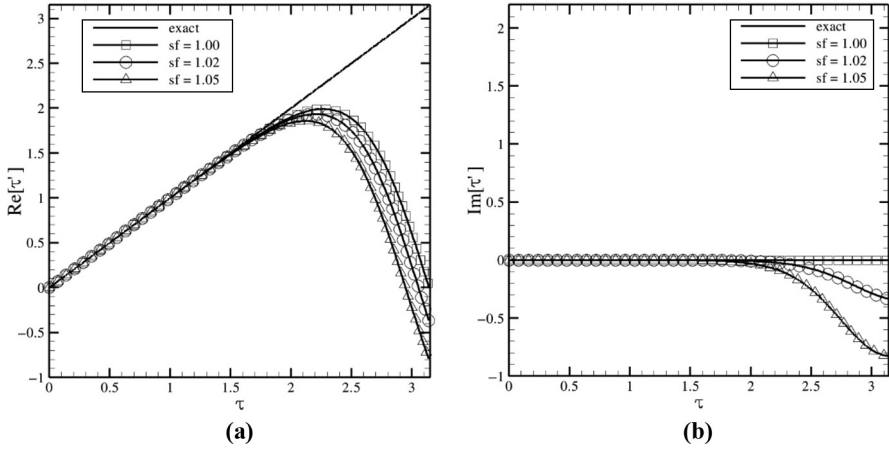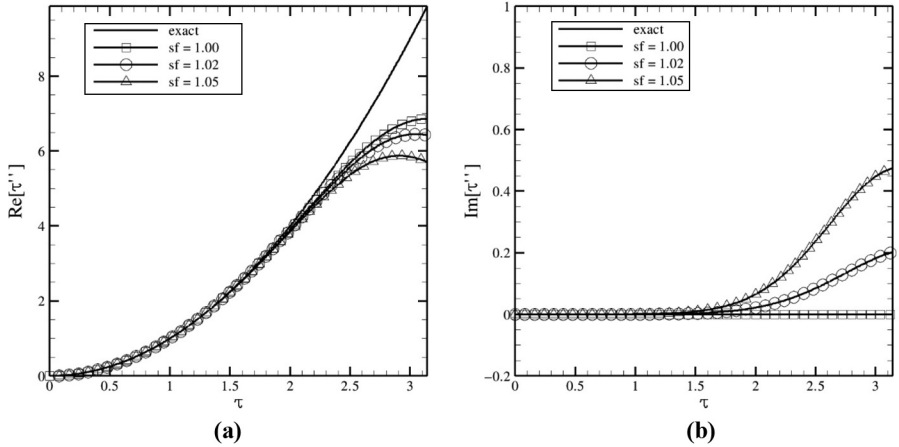
3.4 Boundary approximations for the first and second derivatives

Numerical approximations near the boundaries are generally non-central and non-periodic. In this sense, resolution characteristics for such type of approximations should be considered in only a heuristic level (Lele, 1992). For the first-derivative calculations, stencils for the boundary (first point – f) and next to the boundary (second point – s) are here taken as follows:

$$
\alpha_k^{(f)} f_k' + \alpha_{k+1}^{(f)} f_{k+1}' + a_k^{(f)} f_k + a_{k+1}^{(f)} f_{k+1} + a_{k+2}^{(f)} f_{k+2} \\
+ a_{k+3}^{(f)} f_{k+3} + a_{k+4}^{(f)} f_{k+4} = 0,
\tag{46}
$$

and:

$$
\alpha_{k-1}^{(s)} f_{k-1}' + \alpha_k^{(s)} f_k' + \alpha_{k+1}^{(s)} f_{k+1}' + a_{k-1}^{(s)} f_{k-1} + a_k^{(s)} f_k + a_{k+1}^{(s)} f_{k+1} \\
+ a_{k+2}^{(s)} f_{k+2} + a_{k+3}^{(s)} f_{k+3} + a_{k+4}^{(s)} f_{k+4} = 0.
\tag{47}
$$

www.m

By the use of these two stencils, it is possible to obtain fifth- and sixth-order approximations. Table II presents a set of coefficients for the first derivative cases. Second derivative approximations of the same order can be generated based on the same stencils with an additional coefficient associated with the position $k + 5$. Coefficients for non-centered second-derivative approximations with $sf = 1.00$, 1.02 and 1.05 are presented in Table III.

Spectral resolution analyses of the first-point scheme considering both first and second derivatives are presented in Figures 4 and 5. Moreover, analyses taking into account the first and second derivatives for the second-point scheme are showed in Figures 6 and 7, respectively.

Coefficients	$sf = 1.00$	1.02	1.05
$\alpha_{k-1}^{(f)}$	1	1	1
$\alpha_{k}^{(f)}$	4	3.88388	3.72325
$a_{k}^{(f)}$	3.08333	3.06443	3.03703
$a_{k+1}^{(f)}$	−0.666667	−0.83083	−1.04601
$a_{k+2}^{(f)}$	−3	−2.74499	−2.41269
$a_{k+3}^{(f)}$	0.666667	0.580411	0.473975
$a_{k+4}^{(f)}$	−0.0833333	−0.0690167	−0.523034
$\alpha_{k-1}^{(s)}$	1	1.00051	0.997634
$\alpha_{k}^{(s)}$	6	6	6
$\alpha_{k+1}^{(s)}$	2	2.28768	2.6604
$a_{k-1}^{(s)}$	3.38333	3.38321	3.37543
$a_{k}^{(s)}$	2.5	2.5	2.5
$a_{k+1}^{(s)}$	−6.33333	−6.10104	−5.83625
$a_{k+2}^{(s)}$	0.666667	0.363495	0.0333311
$a_{k+3}^{(s)}$	−0.25	−0.167716	−0.0837953
$a_{k+4}^{(s)}$	0.0333333	0.0220455	0.0112866

Table II. Compact finite difference coefficients for the non-centered first-derivative stencils provided by equations (46) and (47) with $sf = 1.00$, 1.02 and 1.05

Coefficients	$sf = 1.00$	1.02	1.05
$\beta_{k-1}^{(f)}$	780	780	780
$\beta_{k}^{(f)}$	8220	8264.34	8366.46
$b_{k}^{(f)}$	−9775	−9800.96	−9866.53
$b_{k+1}^{(f)}$	20285	20229.7	20177.6
$b_{k+2}^{(f)}$	−11170	−11218.2	−11228.4
$b_{k+3}^{(f)}$	550	755.221	955.328
$b_{k+4}^{(f)}$	145	53.9216	−32.0263
$b_{k+5}^{(f)}$	−35	−19.6781	−5.97994
$\beta_{k-1}^{(s)}$	360	360	360
$\beta_{k}^{(s)}$	4320	4291.93	4265.04
$\beta_{k+1}^{(s)}$	1080	1102.81	1125.51
$b_{k-1}^{(s)}$	−4834	−4812.8	−4790.54
$b_{k}^{(s)}$	8424	8424	8424
$b_{k+1}^{(s)}$	−1890	−2178.65	−2518.42
$b_{k+2}^{(s)}$	−2320	−1886.49	−1399.99
$b_{k+3}^{(s)}$	810	581.935	355.846
$b_{k+4}^{(s)}$	−216	−144.223	−78.8998
$b_{k+5}^{(s)}$	26	16.2172	8.00536

Table III. Compact finite difference coefficients for the non-centered second-derivative stencils provided by stencils similar to equations (46) and (47) with $sf = 1.00$, 1.02 and 1.05

Figure 4.
First derivative real (a)
and imaginary (b)
wavenumber analysis
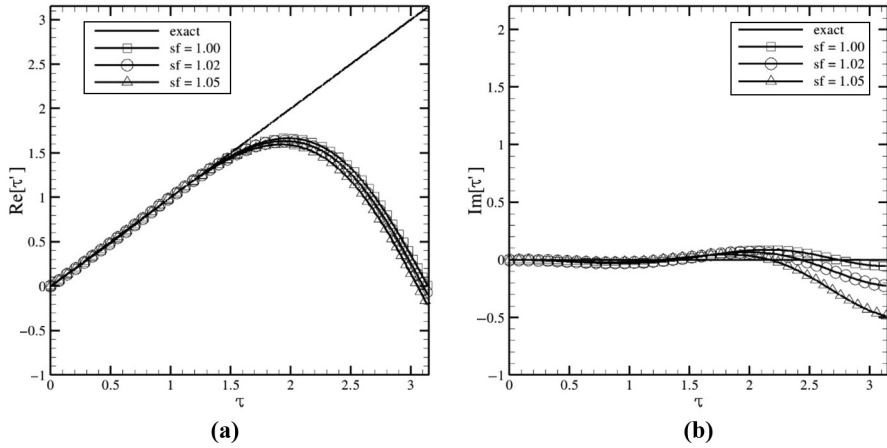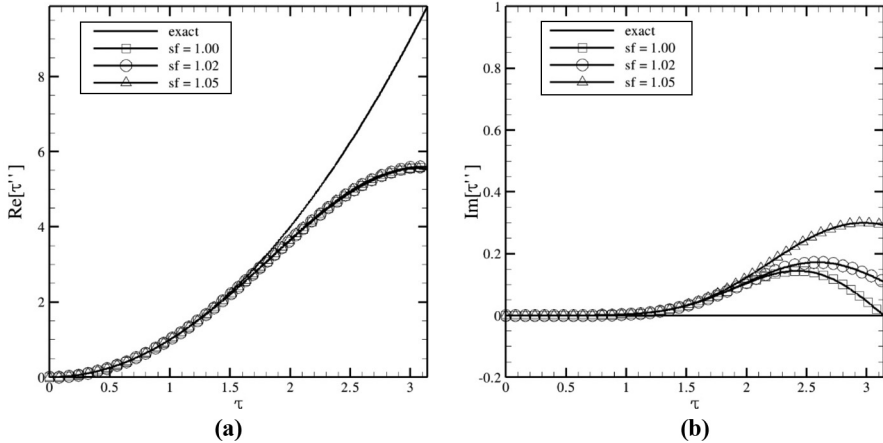of a full non-centered
compact stencil
[equation (46)]

Figure 5.
Second derivative real
(a) and imaginary (b)
wavenumber analysis
of a full non-centered
compact stencil
[similar to equation
(46)]

Although Figures 4-7 have only a heuristic approach, the present analyses are good in showing that the use of small stretching factors preserves the shape of the modified wavenumber for all the non-centered schemes here discussed.

3.5 Verification

The numerical verification and validation of the hydrodynamic code was performed by Souza *et al.* (2004). The adopted code was also verified and the model was validated in cases where no curvature is considered (Petri *et al.*, 2015). Regarding the heat transfer analysis, the verification is performed by comparing our numerical results with the ones provided by Liu and Lee (1995). Dimensional parameters are in accordance with the experiments of Swearingen and Blackwelder (1987). The wall curvature is $R = 3.2\ m$ and the freestream velocity is $U_\infty = 5\ m.s^{-1}$. The characteristic length adopted is $L = 0.1\ m$. The Reynolds number based on this characteristic length is Re = 33,124. It is considered as $\lambda_z = 1.8 \times 10^{-2}\ m$, which corresponds to a nondimensional wavenumber of $\beta = 34.90$.

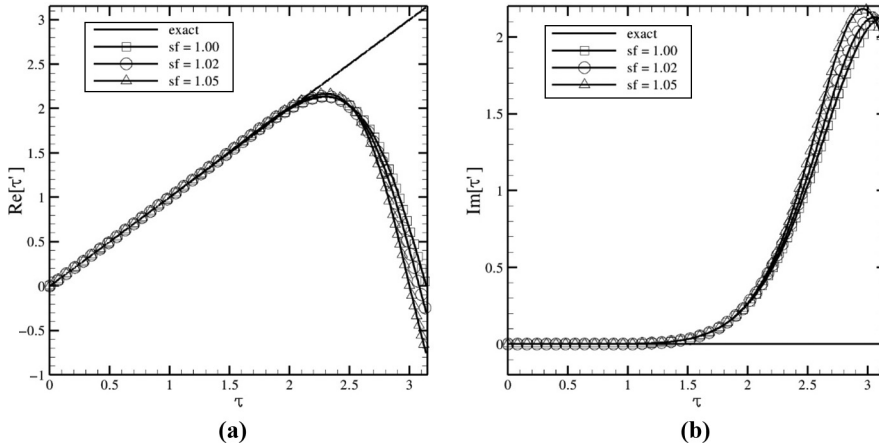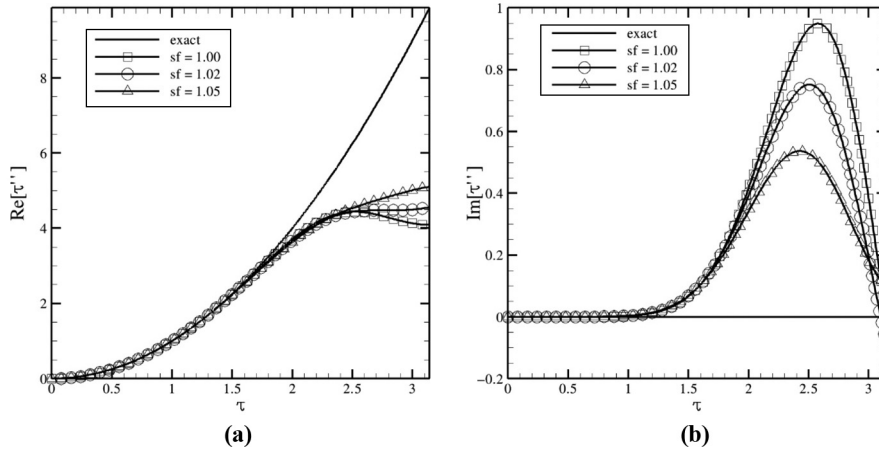Comparison is carried out in terms of heat transfer rates. They are here represented by the Nusselt number normalized by the corresponding value of the Blasius laminar boundary layer. The Nusselt number (Nu_x) is giving by the following equation:

$$Nu_x = q_{wall}\frac{x}{k(T_0 - T_\infty)},\tag{48}$$

where q_{wall} is the heat flux at the wall as follows:

$$q_{wall} = -k\frac{\partial T}{\partial y}\Big|_{wall}.\tag{49}$$

Figure 8 shows spanwise distributions of local surface heat transfer rates for $Pr = 0.72$ at three different streamwise positions. A good agreement between the results of the current

study and those in the literature can be observed. Figure 9 shows the result obtained for Pr = 7.07. Some deviations can be observed in the downwash region because of a better numerical resolution obtained by our code. One may also observe agreement with the literature in the upwash region.

4. Results

The adopted parameters in the following simulations are as follows: $U_\infty = 3\,m.s^{-1}$, $\nu = 1.57 \times 10^{-5}\,m^2.s^{-1}$, Re = 38,336; $Go = 2.389$ and $Pr = 0.72$. The set of physical parameters is in agreement with that mentioned by Mitsudharmadi *et al.* (2004, 2005 2006). The disturbances are introduced in the region $1.049 \leq x \leq 1.1715$ with constant $A = 6 \times 10^{-3}$.

Figure 8.
Local spanwise distribution of the Nusselt number, normalized by the corresponding Blasius–Pohlhausen flat-plate value at the same respective Prandtl number $Pr = 0.72$ (x from 40 to 120 cm; $\Delta x = 40$ cm)
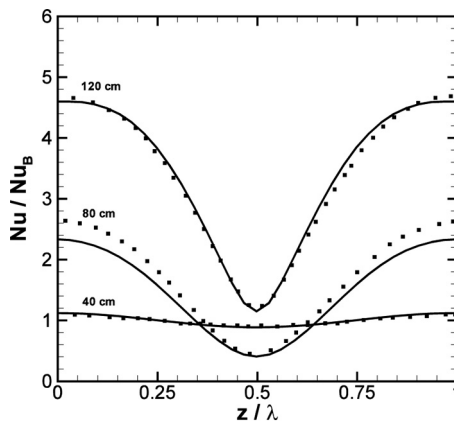
Source: Symbols represent data extracted from and Lee (1995)

Figure 9.
Local spanwise distribution of the Nusselt number, normalized by the corresponding Blasius–Pohlhausen flat-plate value at the same respective Prandtl number $Pr = 7.07$ (x from 40 to 120 cm; $\Delta x = 40$ cm)
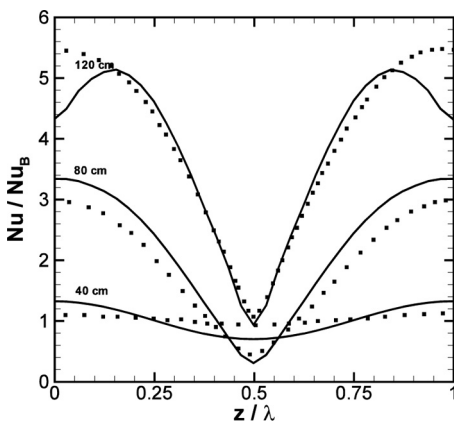
Source: Symbols represent data extracted from Liu and Lee (1995)

Case	Nx	dx	Ny	dy	sf	$K+1$
C1	793	5.197×10^{-3}	201	4.0×10^{-4}	1.01	7
C2	793	5.197×10^{-3}	201	4.0×10^{-4}	1.01	9
C3	793	5.197×10^{-3}	201	4.0×10^{-4}	1.01	11
C4	601	6.86×10^{-3}	121	8.0×10^{-4}	1.01435	11
C5	793	5.197×10^{-3}	121	8.0×10^{-4}	1.01435	11
C6	1177	3.5×10^{-3}	121	8.0×10^{-4}	1.01435	11
C7	793	5.197×10^{-3}	161	6.0×10^{-4}	1.010725	11

Table IV.
Grid independency
test cases.

Notes: In the $(C1 - C2 - C3)$ cases, we increase Fourier mode resolution; the $(C4 - C5 - C6)$ case provides streamwise step-size variation; the $(C3 - C5 - C7)$ cases differ by $y-$resolution.

A mesh refinement test was performed to check the grid independency. Three main groups were considered in accordance with parameters provided by Table IV. With the first group formed by $(C1 - C2 - C3)$ cases, the influence of the Fourier modes was investigated. The investigation of the streamwise step-size dx was conducted by the second group, formed by $(C4 - C5 - C6)$ cases. With the group formed by $(C3 - C5 - C7)$ cases, the variation of the wall-normal step-size dy was verified. For comparison, the $y -$ maximum of the spanwise root mean square (RMS) of both the streamwise velocity component and the temperature distribution is considered as a metric.

In Figure 10, the maximum values of the RMS metric are provided for the first group. Full lines represent the evolution of the streamwise velocity component and the dashed lines denote the temperature evolution. In Figures 11 and 12, the metrics are provided for the second and third groups, respectively.

There are no observable differences between the results when comparing the group formed by $C1$, $C2$ and $C3$ cases (Figure 10). In Figure 11, the same conclusion may be observed for the group formed by $C4$, $C5$ and $C6$ cases. For the group formed by $C3$, $C5$ and $C7$ cases (Figure 12), it can be observed that the mesh refinement in the wall-normal direction can affect the results. However, it can be noticed, by this group comparison, that the results lead to the $C3$ case.

Simulations are performed by considering meshes finer than the ones provided by Malatesta et $al.$ (2013). The adopted mesh parameters are also finer or equal to the finest parameters mentioned in Table IV. An investigation regarding the parallelization independency was conducted in the development phase of the adopted code. Results provided were independent from the number of processing elements considered.
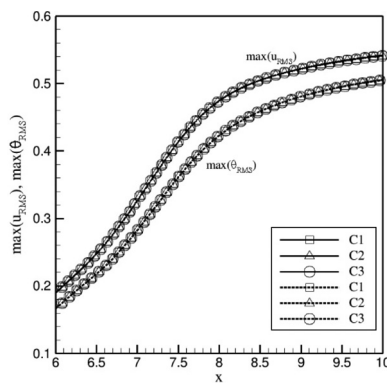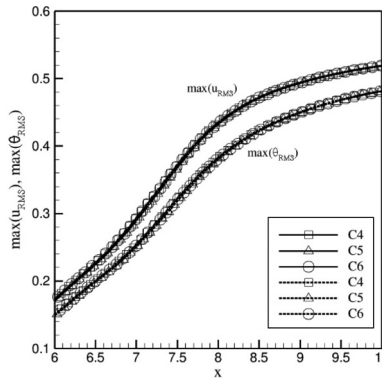

Figure 10.
The $y -$ maximum of the spanwise RMS of both the streamwise velocity component (full lines) and the temperature distribution (dashed lines) for the group formed by $(C1 - C2 - C3)$ cases

In all simulations, the computational domain is divided in the streamwise direction into $N = 8$ parts. The distance between two consecutive points in the x direction is $dx = 3.5 \times 10^{-3}$. In the wall-normal direction, the first distance between consecutive points is $dy = 4 \times 10^{-4}$ and a stretching factor of 1 per cent was adopted. The number of points in the x and y directions are $Nx = 1177$ and $Ny = 201$, respectively; the time step is $dt = 4.3 \times 10^{-4}$. In the z direction, 21 Fourier modes are used with 64 points in the physical space.

The energy is analyzed, and for each Fourier spanwise mode, it is calculated by the following equations:

$$E_k = \int_0^\infty (|U_k|^2 + |V_k|^2 + |W_k|^2)\, dy, \tag{50}$$

for $k > 0$, and:

$$E_k = \frac{1}{2} \int_0^\infty (|U_k|^2 + |V_k|^2)\, dy, \tag{51}$$

for $k = 0$.

Figure 11.
The y−maximum of the spanwise RMS of both the streamwise velocity component (full lines) and the temperature distribution (dashed lines) for the group formed by ($C4 − C5 − C6$) cases

Figure 12.
The y−maximum of the spanwise RMS of both the streamwise velocity component (full lines) and the temperature distribution (dashed lines) for the group formed by ($C3 − C5 − C7$) cases
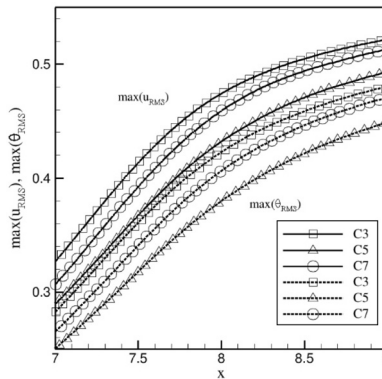
Figure 13 shows the energy development as a function of Re_x for the first 11 Fourier modes. Here $Re_x = U_\infty x/\nu$ can be considered as a streamwise distance from the leading edge. Between the Re_x equals to 5.0×10^4 and 8.0×10^4, the Görtler vortices show a linear growth. Downstream, when their amplitude is already high, nonlinear effects became relevant. The

Figure 13.
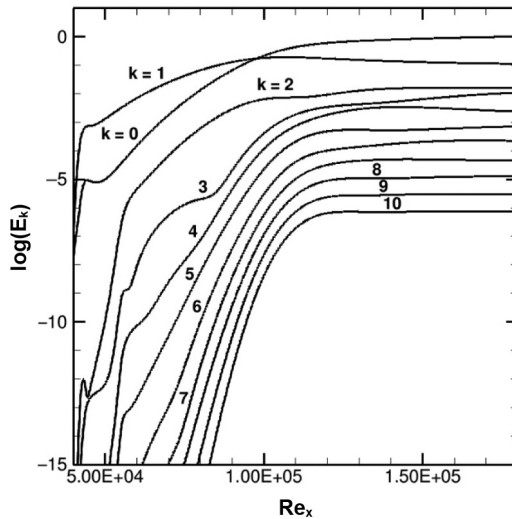Energy distribution
for each Fourier mode
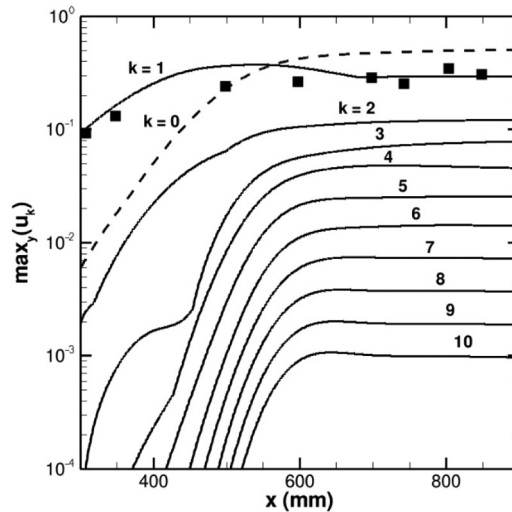in the streamwise
direction

Notes: Full lines represent our numerical results,
and symbols represent experimental ones from
Mitsudharmadi *et al.* (2004)

Figure 14.
Distribution of
maximum disturbance
amplitude shows the
nonlinear growth of
vortices in the
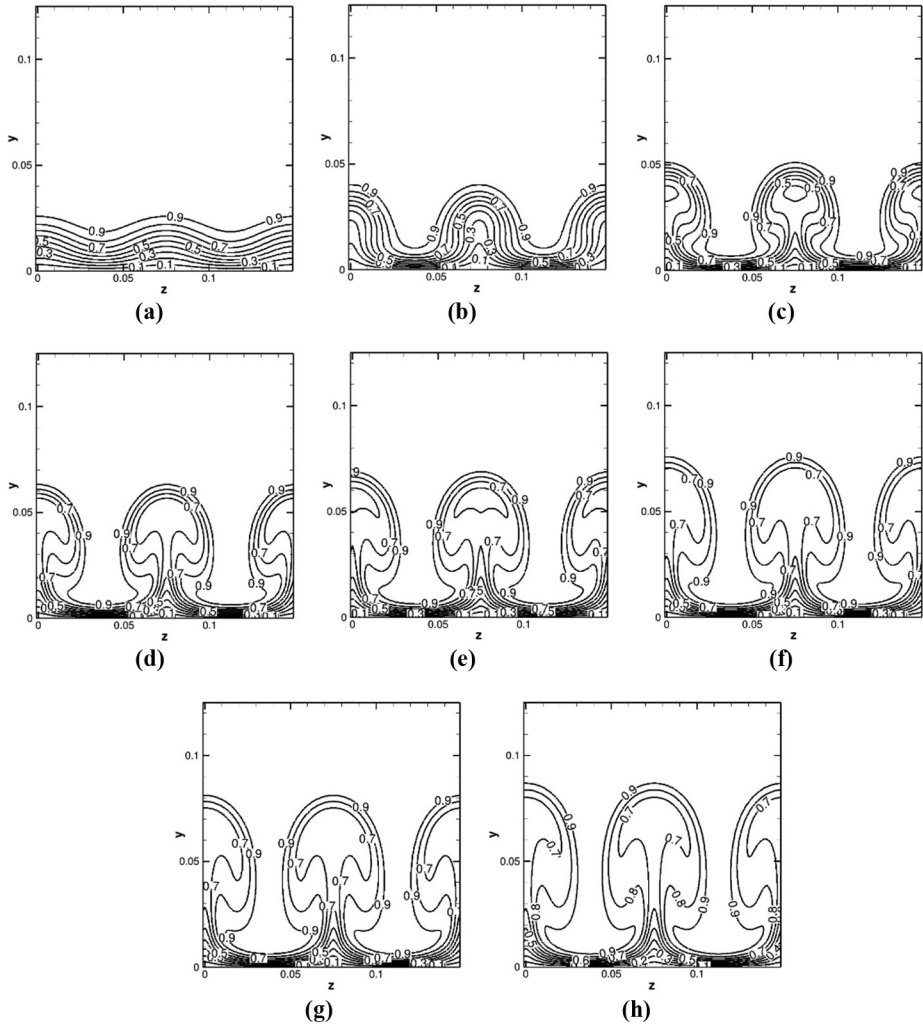boundary-layer flow
on a concave surface

Figure 15.
Crosscut planes ($y \times z$)
of the streamwise
velocity for different
streamwise positions

Notes: (a) – 350 mm; (b) – 500 mm; (c) – 600 mm; (d) – 700 mm; (e) – 745 mm;
(f) – 805 mm; (g) – 850 mm; (h) – 904 mm

nonlinear region is characterized by the formation of a mushroom-like structure in the
crosscut plane ($y \times z$). After $Re_x = 1.0 \times 10^5$, the vortices saturate, i.e. almost all modes
remain with a constant amplitude.

In Figure 14, the development of the maximal disturbance velocity U_{max} for each spanwise
mode is also presented as a function of the dimensional streamwise position. The data are
made dimensional to allow comparison with the experimental data from Mitsudharmadi
et al. (2004). One can observe accordance between the numerical (full line) and the
experimental data (square symbols) for the fundamental mode.

The contours of the streamwise velocity in crosscut planes ($y \times z$) are presented in Figure 15 (a)-(h). In Figure 15(a), one may notice inflections in the velocity profile generated by the presence of the Görtler vortices. From Figure 15(b)-(h), both upwash and downwash regions can be clearly observed.

The streamwise evolution of the spanwise-average Stanton number (St_x) is showed in Figure 16. The spanwise-average Stanton number is calculated by the sum of the Stanton number at each spanwise grid position divided by the total number of points in this direction. Stanton distributions in the upwash (represented by triangles in the Figure 16) and downwash regions (represented by delta symbols) are also presented in Figure 16. Both laminar and turbulent theoretical curves are presented for comparison. In the linear region, one may notice that the spanwise-average Stanton number follows the laminar Stanton distribution as follows:

$$St_{laminar} = 0.453\, Pr^{-0.667} Re_x^{-0.5}$$

It can be observed that, after $Re_x \approx 4.0 \times 10^4$, the Görtler flow intensifies the heat transfer. At $Re_x = 1.8 \times 10^5$, one may observe that the transitional flow reaches Stanton numbers at 393 and 123 per cent higher than laminar and turbulent flows, respectively. The turbulent Stanton distribution is represented by the following function:

$$St_{turbulent} = 0.029 Pr^{-0.57} Re_x^{-0.2}.$$

5. Conclusion

The described numerical simulation technique provided to be a robust and an easy alternative aimed to effectively investigate heat transfer properties in transition flows over concave surfaces with spanwise periodicity. The use of stretched, high-order, compact finite difference approximations showed to be a reliable alternative to reduce the number of
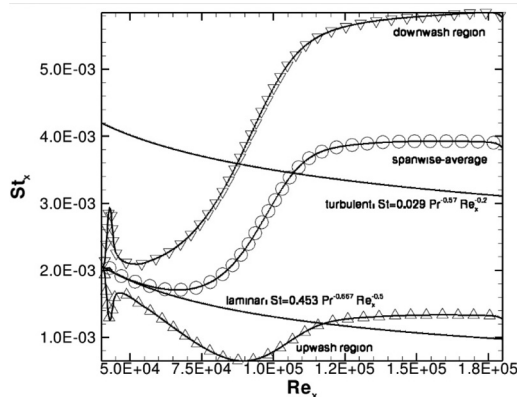
Notes: Gradient symbols represent the streamwise Stanton distribution in the downwash region. The upwash region is represented by triangles. Laminar and turbulent theoretical approximations are also presented for comparison

Figure 16.
The streamwise evolution of the spanwise-averaged Stanton number

discretization points and to preserve grid resolution in the boundary layer region. The numerical procedure is successfully verified. We support literature conclusions in which the transition phenomena may increase heat transfer rates above the laminar and turbulent flow regimes. We strongly believe that the study of the influence of the Görtler flow on the development of secondary instabilities is a natural and important extension of the described study.

References

Biegger, C. and Weigand, B. (2015), "Flow and heat transfer measurements in a swirl chamber with different outlet geometries", *Experiments in Fluids*, Vol. 56 No. 4.

Fiebig, I.H.M. (1996), "Vortices and heat transfer", *Zeitschrift fur Angewandte Mathematik und Mechanik*, Vol. 77 No. 1, pp. 1-16.

Floryan, J.M. (1991), "On the Görtler instability of boundary layers", *Progress in Aerospace Sciences*, Vol. 28 No. 3, pp. 235-271.

Floryan, J.M. and Saric, W.S. (1982), "Stability of Görtler vortices in boundary layers", *AIAA Journal*, Vol. 20, pp. 316-324.

Gamet, L., Ducros, F., Nicoud, F. and Poinsot, T. (1999), "Compact finite difference schemes on non-uniform meshes", *Application to Direct Numerical Simulation of Compressible Flows, International Journal for Numerical Methods in Fluids*, Vol. 29, pp. 159-191.

Hall, P. (1982), "Taylor-Görtler vortices in fully developed or boundary layer flows: linear theory", *Journal of Fluid Mechanics*, Vol. 124, pp. 475-494.

Kloker, M., Konzelmann, U. and Fasel, H. (1993), "Outflow boundary conditions for spatial Navier-stokes simulations of transition boundary layers", *AIAA Journal*, Vol. 31 No. 4, pp. 620-628.

Lele, S.K. (1992), "Compact finite difference schemes with spectral like resolution", *Journal of Computational Physics*, Vol. 103 No. 1, pp. 16-42.

Liu, J.T.C. (2008), "Nonlinear Instability of developing streamwise vortices with applications to boundary layer heat transfer intensification thought an extended Reynolds analogy", *Philosophical Transactions of the Royal Society*, Vol. 366, pp. 101-112.

Liu, J.T.C. and Lee, K. (1995), "Heat transfer in a strongly nonlinear spatially developing longitudinal vortices system", *Physics of Fluids*, Vol. 7, pp. 559-599.

Malatesta, V., Souza, L.F. and Liu, J.T.C. (2013), "Influence of Görtler vortices span wise wavelength on heat transfer rates", *Computational Thermal Sciences: An International Journal*, Vol. 5, pp. 389-400.

Meitz, H.L. (1996), "Numerical investigation of suction in a transition flat-plate boundary layer", PhD thesis, University of Arizona.

Meitz, H.L. and Fasel, H. (2000), "A compact-difference scheme for the Navier–Stokes equations in vorticity-velocity formulation", *Journal of Computational Physics*, Vol. 157 No. 1, pp. 371-403.

Mitsudharmadi, H., Winoto, S.H. and Shah, D.A. (2004), "Development of boundary-layer flow in the presence of forced wavelength Görtler vortices", *Physics of Fluids*, Vol. 16.

Mitsudharmadi, H., Winoto, S.H. and Shah, D.A. (2005), "Secondary instability in forced wavelength Görtler vortices", *Physics of Fluids*, Vol. 17.

Mitsudharmadi, H., Winoto, S.H. and Shah, D.A. (2006), "Development of most amplified wavelength Görtler vortices", *Physics of Fluids*, Vol. 18.

Momayez, L., Dupont, P., Delacourt, G., Lottin, O. and H. Peershossaini (2009), "Genetic algorithm based correlations for heat transfer calculation on concave surfaces", *Applied Thermal Engineering*, Vol. 29, pp. 3476-3481.

Momayez, L., Dupont, P. and Peershossaini, H. (2004), "Effects of vortex organization on heat transfer enhancement by Görtler instability", *International Journal of Thermal Sciences*, Vol. 43 No. 8, pp. 753-760.

Momayez, L. and Peershossaini, H. (2004), "Some unexpected effects of wavelength and perturbation strength on heat transfer enhancement by Görtler instability", *International Journal of Heat and Mass Transfer*, Vol. 47, pp. 495-492.

Peerhossaini, H. (1987), "L'Instabilite d'une Couche Limite Sur Une Paroi Concave Les Tourbilons de Görtler", PhD thesis, University Pierre et Marie Curie, Paris.

Petri, L.A., Sartori, P., Rogenski, J.K. and Souza, L.F. (2015), "Verification and validation of a direct numerical simulation code", *Computer Methods in Applied Mechanics and Engineering*, Vol. 291, pp. 266-279.

Rogenski, J.K., Petri, L.A. and Souza, L.F. (2014), "Effects of parallel strategies in the transition flow investigation", *Journal of the Brazilian Society of Mechanical Sciences and Engineering*, pp. 1-12.

Saric, W.S. (1994), "Görtler vortices", *Annual Review of Fluid Mechanics*, Vol. 26, pp. 379-409.

Saffmann, P.G. (1995), *Vortex Dynamics*, Cambridge University Press, Cambridge.

Schrader, L., Brandt, L. and Zaki, T.A. (2011), "Receptivity instability and breakdown of Görtler flow", *Journal of Fluid Mechanics*, Vol. 682, pp. 362-396.

Souza, L.F., Mendonça, M.T., Medeiros, M.A.F. and Kloker, M. (2004), "Seeding of Görtler vortices through a suction and blowing strip", *Journal of the Brazilian Society of Mechanical Sciences*, Vol. 26, pp. 269-279.

Souza, L.F., Mendonça, M.T. and Medeiros, M.A.F. (2005), "The advantages of using high-order finite differences schemes in laminar-turbulent transition studies", *Numerical Methods in Fluids*, Vol. 48 No. 5, pp. 565-582.

Stüben, K. and Trottenberg, U. (1981), "Nonlinear multigrid methods, the full approximations scheme", *Lectures Notes in Mathematics*, Vol. 5, pp. 58-71.

Swearingen, J. and Blackwelder, R. (1987), "The growth and breakdown of streamwise vortices in the presence of a wall", *Journal of Fluid Mechanics*, Vol. 182, pp. 255-290.

Tandiano, S., Winoto, H. and Shah, D.A. (2009), "Wall shear stress in Görtler vortex boundary layer flow", *Physics of Fluids*, Vol. 21.

209

Corresponding author
Leandro Franco de Souza can be contacted at: lefraso@icmc.usp.br

الاستشارات